

---

This is an electronic reprint of the original article.  
This reprint may differ from the original in pagination and typographic detail.

Das, Suchandrima; Sand, Andrea; Hofmann, Felix

## Dislocation pinning in helium-implanted tungsten : A molecular dynamics study

*Published in:*  
Journal of Nuclear Materials

*DOI:*  
[10.1016/j.jnucmat.2024.155293](https://doi.org/10.1016/j.jnucmat.2024.155293)

Published: 01/12/2024

*Document Version*  
Publisher's PDF, also known as Version of record

*Published under the following license:*  
CC BY

*Please cite the original version:*  
Das, S., Sand, A., & Hofmann, F. (2024). Dislocation pinning in helium-implanted tungsten : A molecular dynamics study. *Journal of Nuclear Materials*, 601, 1-12. Article 155293.  
<https://doi.org/10.1016/j.jnucmat.2024.155293>

---

This material is protected by copyright and other intellectual property rights, and duplication or sale of all or part of any of the repository collections is not permitted, except that material may be duplicated by you for your research use or educational purposes in electronic or print form. You must obtain permission for any other use. Electronic or print copies may not be offered, whether for sale or otherwise to anyone who is not an authorised user.

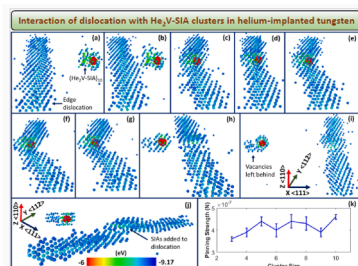


Short communication

# Dislocation pinning in helium-implanted tungsten: A molecular dynamics study

Suchandrima Das<sup>\*,a</sup>, Andrea Sand<sup>b</sup>, Felix Hofmann<sup>c</sup><sup>a</sup> Department of Mechanical Engineering, University of Bristol, Bristol, UK<sup>b</sup> Department of Applied Physics, Aalto University, Finland<sup>c</sup> Department of Engineering Science, University of Oxford, Oxford, UK

## GRAPHICAL ABSTRACT



## ARTICLE INFO

## Keywords:

Molecular dynamics  
Micromechanics  
Plasticity  
Hardness  
Helium-implanted tungsten  
Dislocation mobility

## ABSTRACT

Using molecular dynamics simulations, we investigate the interaction of edge dislocations with He-filled Frenkel pairs (He<sub>2</sub>V-SIA), the predominant defect type in helium-implanted tungsten. Clusters of 3–10 He<sub>2</sub>V-SIA are seen to be stable with their pinning strength increasing with size. For all cluster sizes, the dislocation bows around the cluster and unpins while carrying SIAs with it. The helium-vacancy complex and new vacancies left behind, have little pinning effect, explaining the “defect-clearing” and experimentally observed deformation softening. The predicted solute hardening for 3000 apm helium-induced defect distribution of varying sizes, is in excellent agreement with previous experimental observations.

## Introduction

Tungsten is the leading candidate for armour components in future fusion reactors [1–3]. In-service, irradiation with neutrons and helium will induce material property changes [4–16]. Investigating tungsten implanted with helium at room temperature enables examination of helium-induced damage with minimal evolution, as vacancies in tungsten are effectively immobile below ~600 K [17,18]. Experimental

analysis using thermal desorption spectroscopy [19], nuclear reaction analysis [20] and positron annihilation spectroscopy [21] revealed strongly bound helium-vacancy clusters in such samples. Unfortunately, transmission electron microscope (TEM) is not sufficiently sensitive to image these defects [6,22]. Monochromatic X-ray diffraction (XRD) measurements combined with density functional theory (DFT) calculations predicts such defects to consist of di-helium vacancy complexes bound to a self-interstitial (SIA) (He<sub>2</sub>V-SIA) [5,13,23,24].

\* Corresponding author.

E-mail address: [suchandrima.das@bristol.ac.uk](mailto:suchandrima.das@bristol.ac.uk) (S. Das).<https://doi.org/10.1016/j.jnucmat.2024.155293>

Received 12 April 2024; Received in revised form 10 July 2024; Accepted 11 July 2024

Available online 14 July 2024

0022-3115/© 2024 The Authors. Published by Elsevier B.V. This is an open access article under the CC BY license (<http://creativecommons.org/licenses/by/4.0/>).

Though small, helium-induced-defects can significantly alter material properties: Tungsten implanted with 3000 appm of helium (W-3000He) exhibited large lattice strains ( $\sim 10^{-3}$ ) [25], and substantially reduced thermal diffusivity [26]. Nano-indentation on  $\langle 001 \rangle$ -oriented W-3000He showed a  $\sim 70\%$  increase in hardness and slip-step formation around indents [9]. Akin to observations in other irradiated materials [14,27,28], slip channels and localised deformation were found beneath the indents using depth-resolved micro-beam XRD, high-resolution electron backscatter diffraction [14] and TEM.

Based on these observations, we previously developed a crystal plasticity finite element model (CPFE) to simulate deformation behaviour of W-3000He [14]. The formulation hypothesized hardening from  $\text{He}_2\text{V}$ -SIA obstacles, followed by defect removal and strain-softening [9, 14,29]. Assuming a defect removal process involving dissociation of helium from  $\text{He}_2\text{V}$ -SIA and recombination of the vacancy and SIA, the defect pinning strength was calculated [13,14,30]. Predictions from this model agreed well with nano-indentation experiments and captured the orientation-dependence of the nano-indentation response. The model was subsequently extended to self-ion-implanted tungsten [29,31].

While the CPFE model provided a good match to experiments, the precise interaction mechanism between helium-implantation-induced defects and glide dislocations, leading to the observed initial hardening and subsequent strain softening, remains unclear. A thorough understanding of this is essential to predict in-service mechanical property evolution, and to guide the structured design of materials with enhanced irradiation resistance.

This paper uses molecular dynamics (MD) simulations to investigate how glide dislocations interact with helium-implantation-induced defects. The first goal of this study is to provide mechanistic insight into the origin of the initial hardening and subsequent strain softening observed in experiments. The second goal is to predict how macroscopic mechanical material properties are altered by the presence of helium-implantation-induced defects, such that these effects may be faithfully incorporated into larger scale material simulations.

Prior MD studies on irradiation hardening [32–34] focussed on the binding energy of defects to dislocations, migration of defects near dislocations [35] or interaction between pinning interstitial loops and gliding dislocations. Here we probe the nanoscale mechanisms

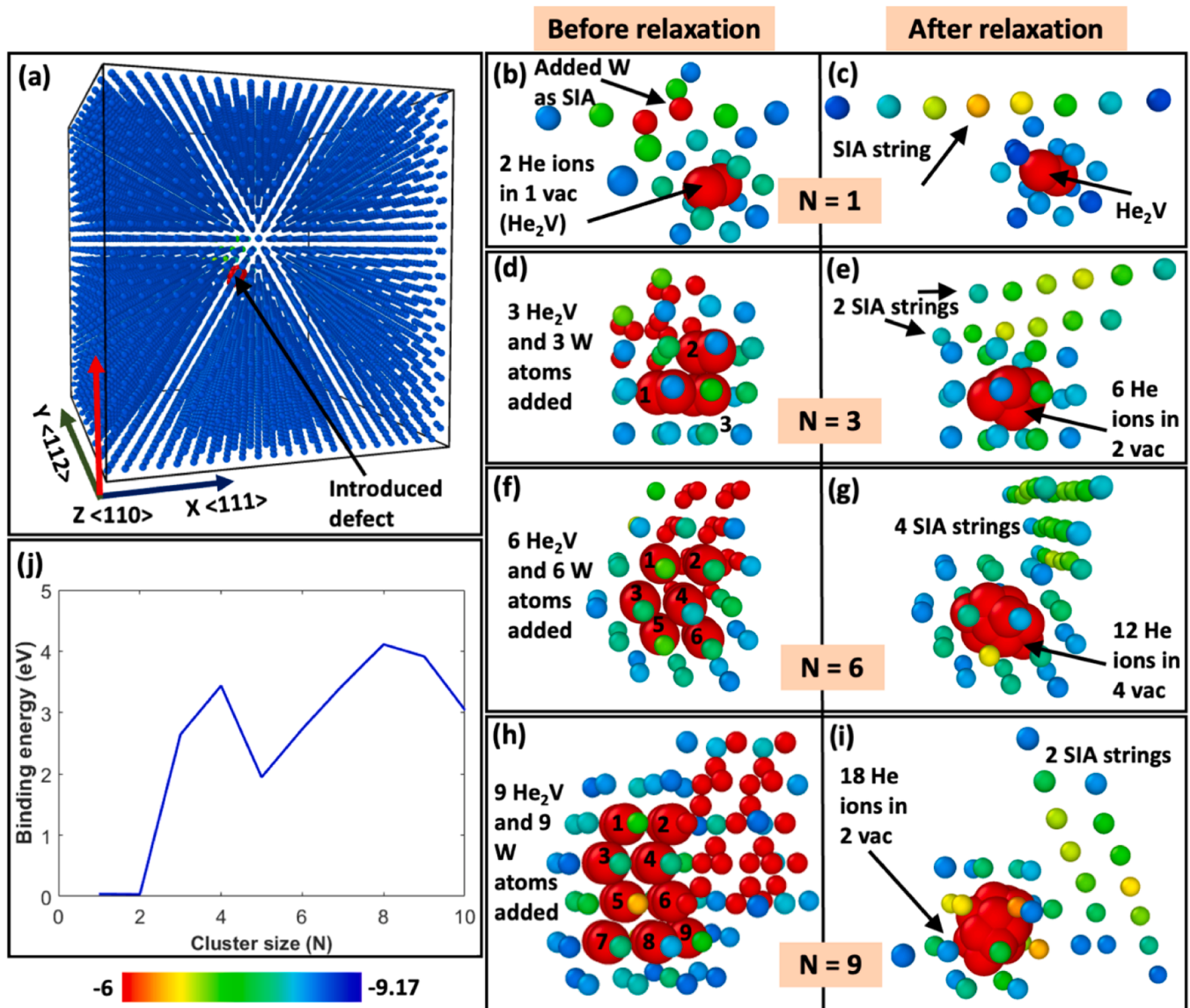


Fig. 1. (a) Cubic tungsten simulation cell (edge dimension  $62 \text{ \AA}$ ) used to examine defect stability. (b) – (i) Examples of formation of  $(\text{He}_2\text{V-SIA})_N$  clusters for varying  $N$ . (j) Binding energy, SIA to  $\text{He}_2\text{V}$ , varying as a function of cluster size. In subplots (a) – (i), tungsten atoms are shown with radius  $0.6 \text{ \AA}$  for ease of visualisation of the helium atoms (shown with radius  $1.22 \text{ \AA}$ ) and the induced defects. Subplots (a) – (i) are coloured according to potential energy (in units of eV) of the individual atoms, with range as indicated in the colour.

underlying the hardening and softening phenomenon by studying the interaction between edge dislocation and He<sub>2</sub>V-SIA clusters at 300 K [5, 13,23,24]. Prismatic interstitial dislocation loops are commonly found in irradiated tungsten and play an important role in controlling the mechanical behaviour of bcc metals under irradiation conditions [36, 37]. Further, MD calculations have shown that indentation in 001 oriented grains in bcc metals, results in the creation of more prismatic loops, composed of edge dislocation segments [38]. Ab-initio calculations for tungsten also reveal that the interaction energy of helium with edge dislocations to be almost twice as large as for screw dislocations [39]. While slow-moving screw dislocations are the rate-limiting factor in unirradiated tungsten, after irradiation, the pinning effect of the defects and consequent hardening should be more prominent for the faster edge dislocations than for the already slow-moving screw dislocations. Thus, here we focus on the interaction between He<sub>2</sub>V-SIA defects and edge dislocations.

The embedded atom potential developed by Bonny et al. [40] was used to simulate a tungsten crystal (lattice constant 3.15 Å, Appendix A) containing helium defects. A viable defect configuration is required to examine interactions with dislocations. A detailed examination of the defect energy landscape is beyond the scope of this study. Thus, possible configurations of the He<sub>2</sub>V-SIA defect were relaxed in an otherwise perfect tungsten cubic cell (edge dimension 62 Å) (Fig. 1(a)) and the binding energy (BE) between the SIA and the He<sub>2</sub>V complex examined to assess its stability.

The He<sub>2</sub>V defect is generated by removing one tungsten atom to create a vacancy, followed by introduction of two helium ions in the vacancy (for a vacancy at co-ordinates [0,0,0], helium ions are introduced at [0.5,0,0] and [-0.5,0,0], (dimensions in Å)). BE is calculated for different positions of the SIA relative to the He<sub>2</sub>V (Appendix B). The highest BE of 0.04 eV is found for the SIA positioned 3.95 Å away from the vacancy in the X and Z directions (XYZ directions in Fig. 1(a)) and 0.78 Å away in the Y direction (configuration in Fig. 1 (b-c)). With such a low BE, this He<sub>2</sub>V-SIA configuration is unstable at 300 K.

Boisse et al. showed that the BE of SIAs with helium-vacancy (He-V) complexes increases with increasing helium in the He-V complex [13]. Becquart et al. suggested that in tungsten the stability of He-V complexes increases with increasing associated vacancies [41]. These observations and our observation of the unstable He<sub>2</sub>V-SIA configuration motivated the search for a configuration made up of clusters of He<sub>2</sub>V-SIA.

To create a cluster of size N, N neighbouring atoms were removed to create N vacancies (neighbouring atoms with co-ordinates within 8 Å in the X, Y and Z directions were chosen (Fig. 1(a)). Relative to each created vacancy, two helium ions and a SIA were introduced. During potential energy minimisation, neighbouring He<sub>2</sub>V-SIA clustered,

causing helium ions to relax into fewer vacancies than originally introduced and allowing recombination of the isolated vacancies with nearby SIAs (Fig. 1 (d-i)). For example, for N = 3, of the three Frenkel Pairs introduced, one was annihilated leaving two SIAs and two vacancies to accommodate the six helium ions.  $1 \leq N \leq 10$  was explored as the induced defects are all below the TEM visibility limit [6]. The results show BE (Appendix B) increases dramatically for N > 2 and stabilises to ~3 eV thereafter (Fig. 1(j)).

The different cluster sizes were equilibrated for 3 ns at 300 K. For N < 3, after a few ps, the SIAs detach from the immobile He<sub>2</sub>V cluster and become mobile. This suggests that for N < 3, the defect clusters are constituted of only helium-vacancy complexes, without a SIA. For N ≥ 3, the defect clusters can be considered to exist in He<sub>2</sub>V-SIA cluster configuration, which is of interest.

Next, we consider the interaction of He<sub>2</sub>V-SIA clusters with an edge dislocation. A simulation cell with an edge dislocation (Burgers' vector  $\frac{1}{2}$  [111] (X-axis), line direction [11 $\bar{2}$ ] (Y-axis) and on slip plane [1 $\bar{1}$ 0] (X-Y plane)) introduced in the middle is considered (Fig. 2(a)). Periodic boundary conditions were applied along the X and Y directions to simulate an infinite array of parallel dislocations and improve the accuracy of defect-dislocation interactions by minimising strain on the dislocation core [42] (Appendix C). The cell dimensions (Fig. 2(a)) were chosen to minimise dislocation-image interactions and to obtain a dislocation density of ~10<sup>15</sup> m<sup>-2</sup>, similar to that generally encountered in plastically deformed metals [43]. The cell contains 944,463 atoms. Two blocks of atoms, at the top (Block A) and bottom (Block B) of the cell (Fig. 2(a)) are kept immobile. The defect cluster is introduced in the path of the dislocation, 150 Å away from it, along the X-axis (Fig. 2(a)). Eight simulations were carried out, for  $3 \leq N \leq 10$ . Following potential energy minimisation, the cell is equilibrated for 250 ps at 300 K. Subsequently, Block B is kept fixed while Block A is displaced to give a constant shear strain rate of 10<sup>-6</sup> ps<sup>-1</sup>. This shear strain rate minimises the rate dependence of pinning strength (Appendix D). The shear stress required to achieve the pre-defined shear strain is continuously recorded until the dislocation passes the defect and reaches the edge of the cell. The shear stress is multiplied with the surface area of the cell's XY face (1.47 × 10<sup>-15</sup> m<sup>2</sup>) (Fig. 2(a)) to obtain the pinning force.

Fig. 2(b) illustrates the pinning effect by considering a cell with and without a defect cluster of size N = 3. It is noted here that observations made from Fig. 2(b) and subsequently from Fig. 3 apply to all  $3 \leq N \leq 10$ . Fig. 2(b) shows the measured pinning force averaged over 100 ps intervals (details in Appendix E). In contrast to a rather flat curve recorded for dislocation glide in a defect-free cell, a clear peak in the curve is noticed in the presence of a (He<sub>2</sub>V-SIA)<sub>3</sub> defect, indicating the

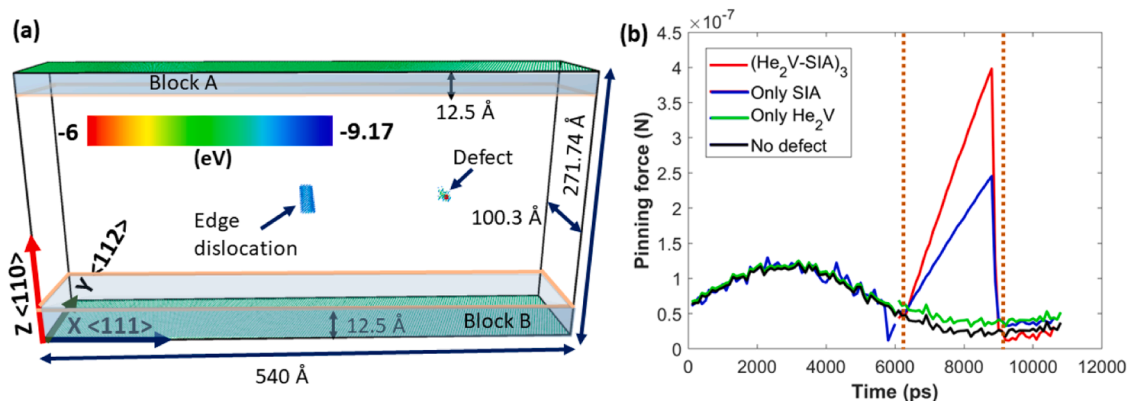


**Fig. 2.** (a) Simulation cell with edge dislocation at the centre and a He<sub>2</sub>V-SIA defect cluster introduced in its path. Atoms in the cell are coloured according to their potential energy (PE) (in units of eV) with range as indicated in the colour-bar. Atoms with PE < -8.7 eV are excluded for ease of visualisation and tungsten atoms are shown with a reduced radius of 0.6 Å. Blocks of atoms above and below the dotted enclosure at the top (block A) and bottom (block B) of cell respectively are kept immobile. (b) Pinning force (averaged over every 100 ps) recorded as the dislocation moves through the cell when block B is kept fixed and block A is sheared at a constant rate of 10<sup>-6</sup> ps<sup>-1</sup>. Plots are shown for a cell with (He<sub>2</sub>V-SIA)<sub>3</sub> defect; a cell with just 2 SIAs; a cell with ((He<sub>2</sub>V)<sub>3</sub>) defect; and a perfect, defect-free cell.

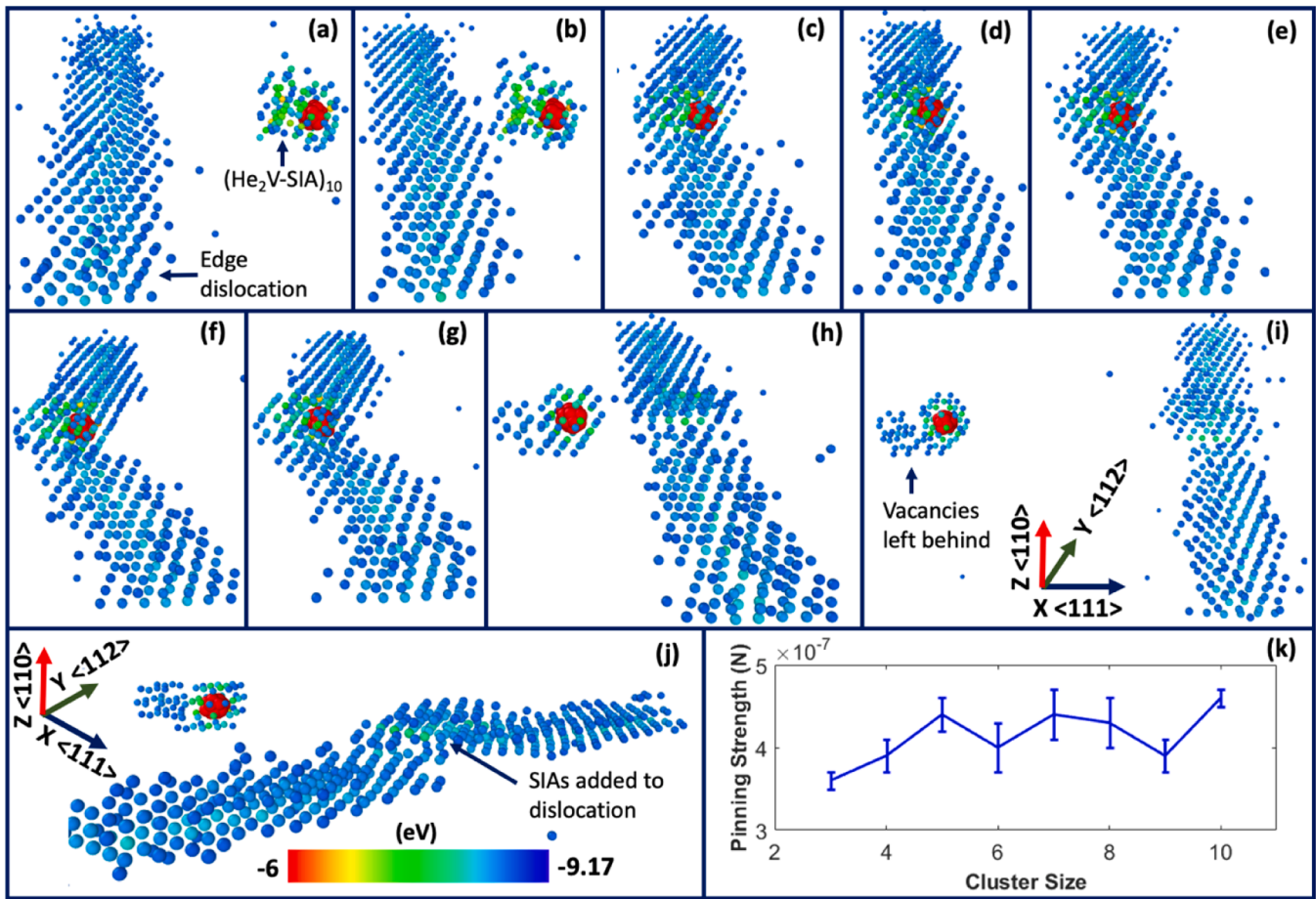


**Fig. 3.** (a) – (i) Subplots showing defect-dislocation interaction as the dislocation encounters a  $(\text{He}_2\text{V-SIA})_{10}$  cluster, gets pinned, bows around the cluster, unpins and moves past. The atoms are coloured according to their potential energy (in units of eV) with range as indicated by the colour-bar. The XYZ co-ordinates in subplot (i) apply to all subplots from (a) – (i). (j) A rotated view of the  $(\text{He}_2\text{V-SIA})_{10}$  cluster and the dislocation after passing through the defect, demonstrating the SIAs added to the dislocation and helium-vacancy complex and newly created vacancies left in the wake of the dislocation. For ease of visualisation, tungsten atoms are shown with a radius of 0.6 Å, and helium atoms with a radius of 1.22 Å. The same defect-dislocation interaction mechanism was observed for cluster sizes 3 to 10. (k) Plot of the pinning strength as a function of cluster size. The error bars represent  $\pm 1$  standard deviation across the values estimated from the measured pinning force data averaged over every 20, 50, 100, 150 and 250 ps respectively.

pinning and unpinning phase. Pinning strength is calculated by subtracting the pinning force for the defect-free case (averaged over the zone demarcated by the orange dotted line in Fig. 2(b)) from the maximum pinning force recorded with the defect present (Table 1). The pinning strength is also calculated by considering the pinning force

curves (such as in Fig. 2(b)) averaged over every 20 ps, 50 ps, 200 ps and 250 ps. The  $\pm 1$  standard deviation across the values for the five averaging periods is the uncertainty in the calculated pinning strength (Fig. 3 (k) and Table 1).

Two further simulations are run with only 2 SIAs (as expected for

**Table 1**

Variation of pinning strength and total solute hardening force with cluster size of  $\text{He}_2\text{V-SIA}$  defects. The uncertainty for the calculated pinning strength ( $F$ ) for each cluster size, is  $\pm 1$  standard deviation across the four values estimated from the measured pinning force data averaged over every 20, 50, 100, 200, 250 ps, respectively. The uncertainty for  $F_{\text{mean}}$  is calculated as  $\pm 1$  standard deviation across the  $F_{\text{tot}}$  values for all the cluster sizes considered. The surface area of the XY face of the simulation box (Fig. 2(a)), used in the computation of  $F_1$  is  $1.47 \times 10^{-15} \text{ m}^2$ . Details of calculation of parameters  $C$  and  $D$  in Appendix F.

Cluster size (N)	Pinning strength (F) in $\mu\text{N}$	Pinning stress $F_1 = F/$ (surface area of XY face of simulation box) (in MPa)	Total no. of helium ions. $A = 2 \times N$	Concentration of clusters for 3000 appm implanted helium $B = (3000/A)$ appm	Spacing between defects considering uniform distribution (C in Å)	No. of defect clusters at any point along slip direction. $D = (100/C)$	Total solute hardening force. $F_{\text{tot}} = D \times F_1$ (MPa)
3	$0.36 \pm 0.01$	$250 \pm 10$	6	500	30.87	3	$750 \pm 30$
4	$0.39 \pm 0.02$	$270 \pm 10$	8	375	33.98	3	$810 \pm 30$
5	$0.44 \pm 0.02$	$300 \pm 10$	10	300	36.61	3	$900 \pm 30$
6	$0.4 \pm 0.03$	$270 \pm 20$	12	250	38.9	3	$810 \pm 60$
7	$0.44 \pm 0.03$	$300 \pm 20$	14	214.59	40.95	2	$600 \pm 40$
8	$0.43 \pm 0.03$	$290 \pm 20$	16	187.5	42.82	2	$580 \pm 40$
9	$0.39 \pm 0.02$	$270 \pm 10$	18	166.67	44.53	2	$540 \pm 20$
10	$0.46 \pm 0.01$	$310 \pm 10$	20	150	46.12	2	$620 \pm 20$
							<b>Mean (<math>F_{\text{mean}}</math>) = <math>700 \pm 124</math></b>

relaxed  $(\text{He}_2\text{V-SIA})_3$  and with only a  $(\text{He}_2\text{V})_3$  defect (introduced at the same co-ordinates as the  $(\text{He}_2\text{V-SIA})_3$  in the dislocation path respectively. For simulation with only SIAs, the cell was equilibrated for 2 ps at 300 K to prevent the mobile SIAs from moving away. It is seen that a  $(\text{He}_2\text{V})_3$  defect, on its own, has almost no pinning effect, while the pinning strength of the SIAs alone is  $\sim 55\%$  that of the  $(\text{He}_2\text{V-SIA})_3$  (Fig. 2(b)). This surprising result shows that the stable bonding of SIAs to the  $\text{He}_2\text{V}$  cluster makes a substantial contribution to the dislocation pinning effect. This could qualitatively explain the behaviour experimentally observed in nano-indentation measurements, where the increase in hardness in W-3000He ( $\sim 0.2$  dpa) is almost double that of self-

ion implanted tungsten with a five times larger damage level of 1 dpa (exposed at room temperature and with predominantly SIA loop defects) [9,31].

Interestingly, for all cluster sizes ( $3 \leq N \leq 10$ ), the dislocation bows around the cluster, until it gets unpinned, carrying the SIAs with it and leaving behind a helium-vacancy complex and newly created vacancies in its wake (Fig. 3(a) – (i)). The dislocation, which acts as a sink for the SIAs, experiences climb in the process. Since a helium-vacancy complex, without SIA, has no significant pinning effect (Fig. 2(b)), by carrying away the SIAs, the dislocation removes the pinning characteristic of the defects, creating an effectively “defect-free” channel. This explains the

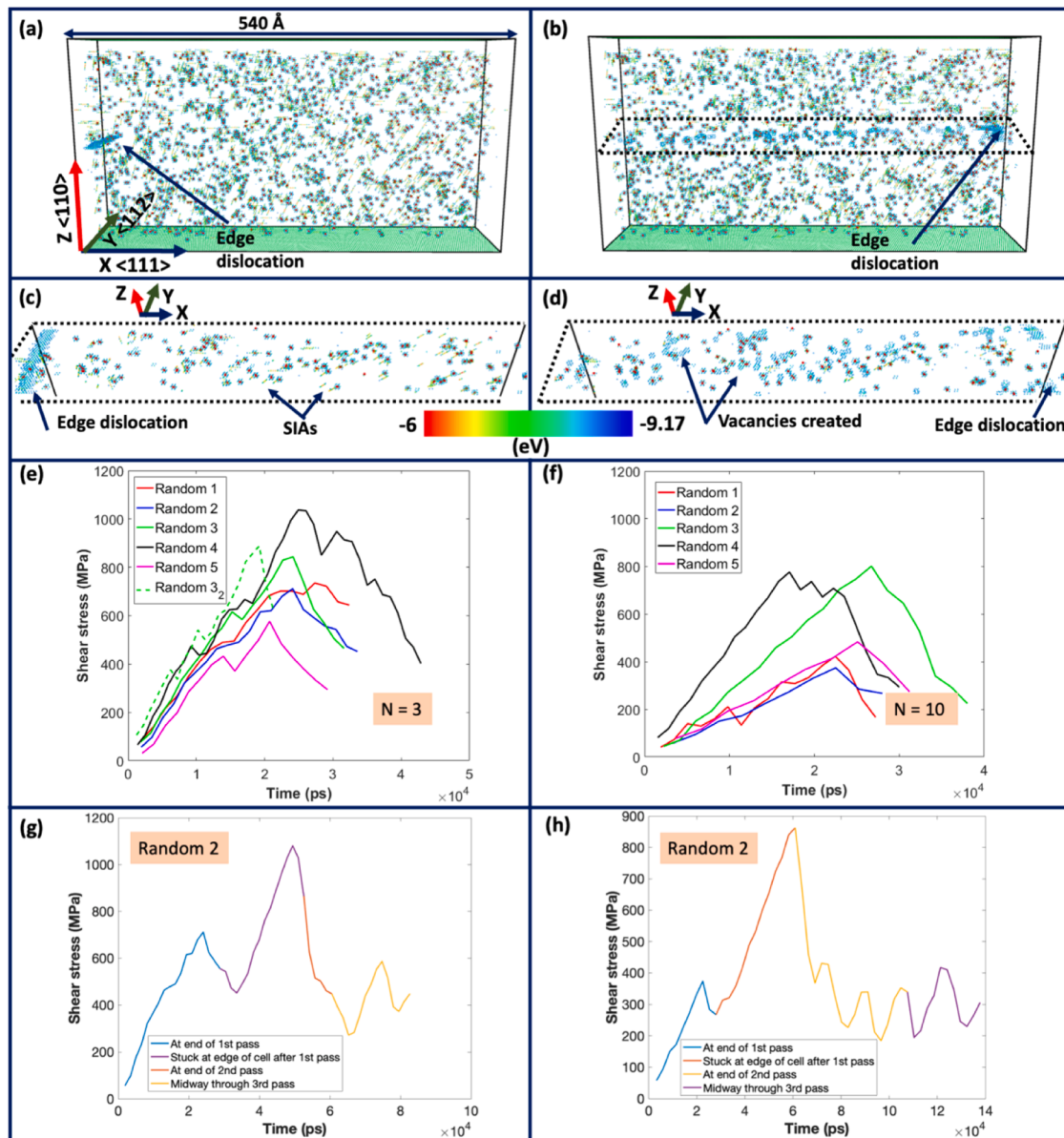


**Fig. 4.** Simulation cell with a random distribution of  $(\text{He}_2\text{V-SIA})_3$  defects (a) Start of the simulation, with the edge dislocation introduced at the edge of the cell (b) End of the simulation, when the dislocation has reached the other edge of the cell. XYZ co-ordinates superimposed on subplot (a) also apply to (b). Isolated view of the XY plane containing the gliding dislocation during the simulation (c) at the beginning showing  $(\text{He}_2\text{V-SIA})_3$  clusters and (d) at the end, when the dislocation has passed through the defects, carrying the SIAs with it and leaving behind the helium-vacancy complexes and newly created vacancies nearby. The XYZ axes superimposed on (c) and (d) have the same directions as in (a). Atoms are coloured according to their potential energy with range indicated by the colour-bar. For ease of visualisation, tungsten atoms are shown with a radius of  $0.6 \text{ \AA}$ , and helium atoms with a radius of  $1.22 \text{ \AA}$  and atoms with potential energy  $< -8.7 \text{ eV}$  are excluded. Shear stress required for an edge dislocation to glide through the simulation cell for five different random distribution of  $(\text{He}_2\text{V-SIA})_N$  defect clusters (e)  $N = 3$  (f)  $N = 10$  (curves averaged over every 100 ps). The “Random  $3_2$ ” curve in subplot (e), is the case for the simulation corresponding to “Random 3” repeated with the dislocation introduced in the middle of the cell. Shear stress required for multiple passage of the dislocation through the simulation cell for a random distribution of  $(\text{He}_2\text{V-SIA})_N$  defect clusters (g)  $N = 3$  (h)  $N = 10$  (curves averaged over every 100 ps).

experimental observation of defect-free channels beneath indents in W-3000He [14]. This observation also suggests an inability of vacancies to pin gliding dislocations. This explains why a previous crystal-plasticity study of self-ion implanted tungsten agreed well with experiments, although only dislocation loops were modelled as obstacles and vacancies ignored [31].

The pinning strength increases slightly with cluster size (Table 1), with a maximum increase of  $\sim 25\%$  (Fig. 3(k)). We have used these to estimate the total solute hardening force experienced by a gliding dislocation when moving through a concentration of such clusters, induced by 3000 appm helium implantation. This can be compared to  $\sim 750$  MPa estimated from previous CPFPE simulations matched to experiments [14].

A first estimate is made by assuming a uniform defect distribution (similar assumption made in CPFPE). To account for the existence of clusters of varying sizes, the total solute hardening force is calculated separately for a uniform distribution of clusters of each size ( $F_{tot}$  in Table 1) followed by taking the average over all cluster sizes. Contrary to pinning strength,  $F_{tot}$  is seen to reduce with increasing cluster size, because of the reduction in cluster number density as  $N$  increases. The average of  $F_{tot}$  for different sizes ( $F_{mean}$ ), is found to be  $\sim 700$  MPa (Table 1). This agrees remarkably well with the estimate of  $\sim 750$  MPa from CPFPE matched to experiments.

The  $F_{tot}$  for different cluster sizes (Table 1), can also be used to estimate the average energy barrier of a defect cluster across the varying examined cluster sizes. This can be calculated by considering  $F_{tot}$ , the number of defects encountered by the dislocation in its glide plane for each considered cluster size and that the simulation box moves over by one Burgers' vector when the dislocation has propagated through the whole length of the simulation cell in the direction of glide i.e.  $540 \text{ \AA}$  in the X direction. Details of the energy calculation can be found in Appendix G. The average energy barrier for a defect across all the examined cluster sizes is found to be  $\sim 0.05 \text{ meV}$  (Table G.1 in Appendix G) corresponding to average solute hardening ( $F_{mean}$ ) of 700 MPa (Table 1).

To further examine  $F_{tot}$  for varying  $N$  (and therefore  $F_{mean}$ ),  $F_{tot}$  is also estimated for  $N = 3$  (500 clusters) and  $N = 10$  (150 clusters) randomly distributed in the simulation cell. For each cluster size five simulations were performed. The dislocation is introduced at one edge of the cell and allowed to propagate along the X direction to the other edge of the cell (Fig. 4(a-b)). Block B is kept fixed while Block A is displaced to give a shear strain rate of  $10^{-6} \text{ ps}^{-1}$  (Fig. 2(a)). Consistent with the single cluster simulations, the dislocation carries away the SIAs of all the clusters it encounters. In its wake, it leaves an SIA-free path, populated with helium-vacancy complexes and a newly created vacancies (Fig. 4(c-d)).

Fig. 4(e-f) shows the shear stress required for the dislocation to glide through each of the five random distributions for  $N = 3$  and  $N = 10$ . One of the random distributions for  $N = 3$  (Random 3) was repeated with the dislocation traversing half the length of the cell (from middle to the edge, Random 3<sub>2</sub>) (Fig. 4(e)). The peak stress for "Random 3" and "Random 3<sub>2</sub>" being within 5 % of each other, confirms that the peak stress is independent of the path-length traversed by the dislocation. Between the random cases, the peak stress reached varies; between  $\sim 374$ – $800$  MPa with an average of 571.59 MPa for  $N = 10$  and between  $\sim 577$ – $1037$  MPa, with an average of 780.78 MPa for  $N = 3$ . For both  $N = 3$ , and  $N = 10$ , one random case is simulated for longer time, allowing the dislocation to undergo multiple passes through the same region in the simulation cell (Random 2 case from Fig. 4(e) and (f) are rerun for longer time). This method representing other dislocations passing sequentially through the same region in the cell is justified by the periodic boundary conditions applied to the cell, which ensures that for each passage, the incoming dislocation is well-aligned with the glide plane. The shear stress was recorded as the dislocation traversed through the cell multiple times (Fig. 4(g) and (h)). The observation shows that there is a sharp drop in the recorded shear stress for the second or subsequent passage of the dislocation through the cell. This shows that

during the first passage, the dislocation cuts through and removes defects in the concerned glide plane, resulting in a relatively defect free channel for passage of subsequent dislocations and consequent strain softening.

The average stress values for  $N = 3$  and  $N = 10$  are within  $\sim 10\%$  of the corresponding  $F_{tot}$  computed from uniform defect distribution (Table 1). Though a quantitative comparison is not justified by 5 random distributions examined for each  $N$ , this qualitative agreement lends credence to the cluster size dependence of  $F_{tot}$  in Table 1.

An interesting feature the simulations show is the pronounced climb of the edge dislocation through absorption of SIAs. The initiation of dislocation climb can be seen in Fig. 3(j), where the dislocation has absorbed the SIA after interacting with one  $(\text{He}_2\text{V-SIA})_{10}$  cluster. Dislocation climb becomes more evident for a dislocation that traverses a cell containing randomly distributed defect clusters (Fig. 4(a) and (b)). Fig. 5 shows that, as the dislocation moves through the distribution of defects, it absorbs more SIAs, causing it to climb out of the glide plane by almost  $\sim 1 \text{ nm}$ .

The climb of edge dislocations through the absorption or emission of point defects, such as vacancies or self-interstitial atoms (SIAs), is a well-known [44]. Generally, the contribution of SIAs to this process is ignored due to their higher formation energy compared to vacancies [45]. Interestingly, our results show the opposite behaviour under irradiation condition: The abundance of SIAs and vacancies created by helium-implantation, together with the specific defect-dislocation interactions observed, results in SIAs playing a pivotal role in facilitating dislocation climb. This agrees with a previous dislocation dynamics study, where the authors concluded that the existence of large concentrations of SIAs due to irradiation enhances dislocation climb which would otherwise only occur at a much higher temperature [45].

Past studies have shown that a combination of glide and climb motion can enhance the overall mobility of dislocations, facilitating annihilation of dislocations and recovery of dislocation structures [46–48]. Dislocation climb can also bring about a reduction in flow stress and reduced hardening for polycrystalline components [49–51]. Overall, enhanced dislocation climb at such low temperatures, induced by irradiation conditions, suggests a substantial loss of material strength.

The present simulations elucidate the mechanisms responsible for the experimentally-observed deformation behaviour; dramatic increase in hardness, followed by softening of helium-ion-implanted tungsten [9]. While individual  $\text{He}_2\text{V-SIA}$  defects and clusters with fewer than three of these defects ( $N < 3$ ) are not stable, we find stable configurations for  $N \geq 3$ . The large pinning strength of  $\sim 0.4 \text{ \mu N}$ , even for  $N = 3$ , leads to an estimated increase in shear strength that is consistent with the  $\sim 75\%$  increase in hardness observed experimentally in nano-indentation of W-3000He [9]. Our findings reveal the following mechanism: gliding dislocations remove SIAs from  $\text{He}_2\text{V-SIA}$  clusters, leaving behind  $\text{He}_2\text{V}$  clusters.  $\text{He}_2\text{V}$  clusters offer little resistance to glide dislocations, thus resulting in the experimentally observed strain softening and formation of easy glide channels. We also observe SIA-assisted dislocation climb at 300 K, which normally only occurs at much higher temperatures. Our results disprove the defect-dislocation interaction mechanism and consequent hardening and softening mechanisms previously hypothesized in our CPFPE model of W-3000He [14]. This underscores the necessity of employing atomistic simulations to establish a mechanistic foundation for larger-scale simulations. Such integrated multi-scale simulations combined with observations from complementary experimental techniques is pivotal in constructing a thorough understanding of material behaviour and its underlying mechanisms.

## Originality statement

I write on behalf of myself and all co-authors to confirm that the results reported in the manuscript are original and neither the entire work, nor any of its parts have been previously published. The authors confirm that the article has not been submitted to peer review, nor has

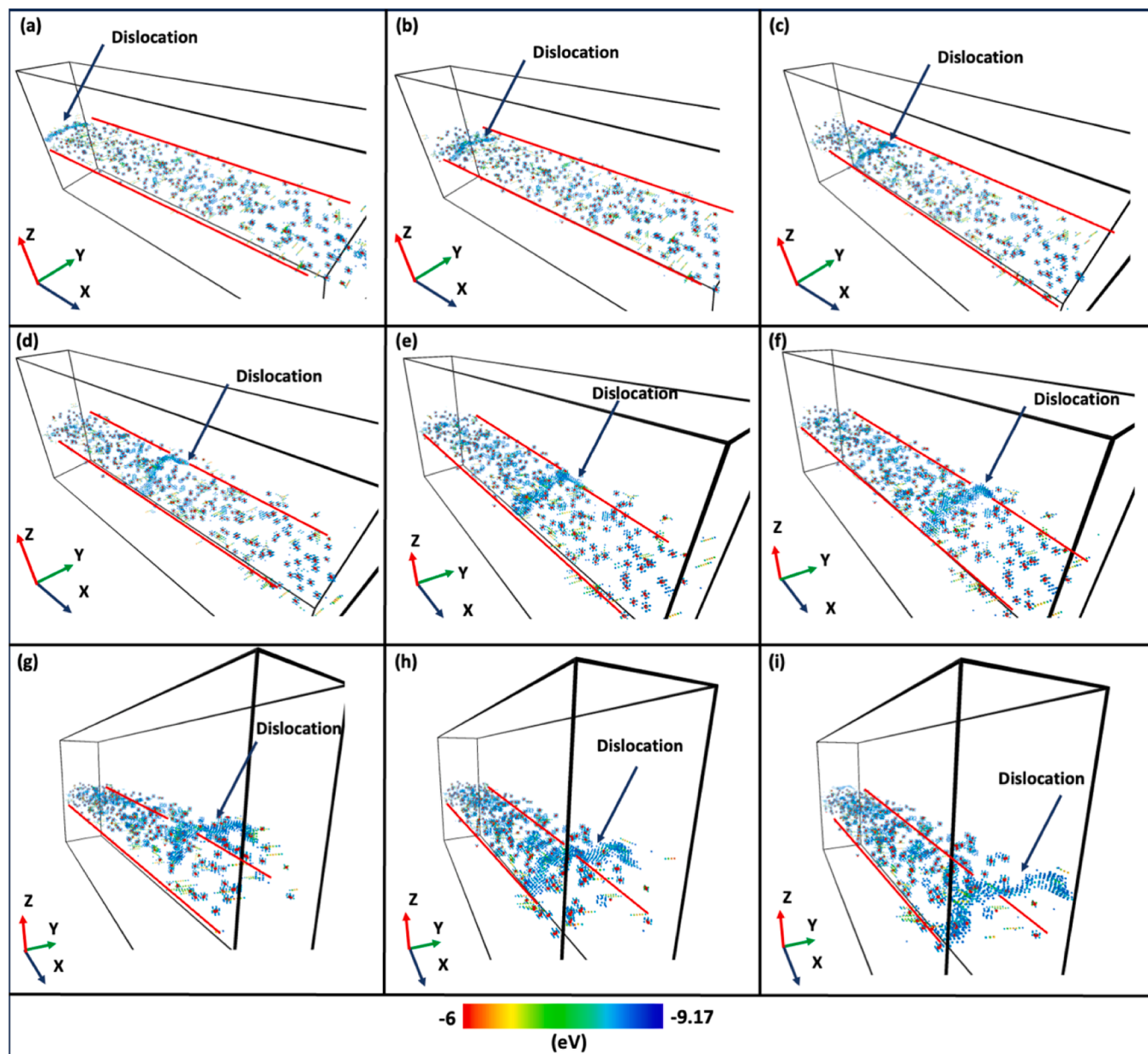


**Fig. 5.** (a) – (i) Snapshots of simulation cell with isolated view of the XY plane containing the dislocation as it glides through a random distribution of  $(\text{He}_2\text{V-SIA})_3$  defects (a) Start of the simulation, with the edge dislocation introduced at the edge of the cell (i) End of the simulation, when the dislocation has absorbed SIAs, leaving behind the helium-vacancy complexes and newly created vacancies nearby, and has undergone climb. Atoms are coloured according to their potential energy with range indicated by the colour-bar. For ease of visualisation, tungsten atoms are shown with a radius of 0.6 Å, and helium atoms with a radius of 1.22 Å and atoms with potential energy  $< -8.7$  eV are excluded.

been accepted for publishing in another journal. The authors confirm that the research in their work is original, and that all the data given in the article are real and authentic. If necessary, the article can be recalled, and errors corrected.

#### Data availability statement

The data that support the findings of this study are available within the article and the appendices. The raw simulation data will be available from the corresponding author upon reasonable request.

#### CRediT authorship contribution statement

**Suchandrima Das:** Writing – review & editing, Writing – original draft, Visualization, Supervision, Software, Methodology, Investigation,

Funding acquisition, Formal analysis, Conceptualization. **Andrea Sand:** Writing – review & editing, Visualization, Software, Methodology, Investigation, Formal analysis. **Felix Hofmann:** Writing – review & editing, Supervision, Project administration, Methodology, Funding acquisition, Conceptualization.

#### Declaration of competing interest

The authors declare that they have no known competing financial interests or personal relationships that could have appeared to influence the work reported in this paper.

#### Acknowledgements

This work was in part supported by the European Research Council

through grant 714697 and in part by Engineering and Physical Sciences Research Council fellowship Reference number EP/N007239/1. We are grateful to Dr. Edmund Tarleton for supporting this work.

## Appendix A

The potential considers the lattice constant of tungsten to be 3.14 Å at 0 K. Since the simulations are intended to be representative of phenomena at 300 K, the lattice constant relevant to this potential at 300 K was determined. For this purpose, a cubic cell, made of tungsten atoms without any defects, with edge dimension of 30 nm, was considered. The cell was allowed to achieve potential energy minimisation, following which it was allowed to equilibrate at 300 K for 600 ps. The lattice constant was recorded throughout the simulation (Fig. 6) and the average taken over the last 300 ps (3.15 Å) was used in all subsequent simulations.

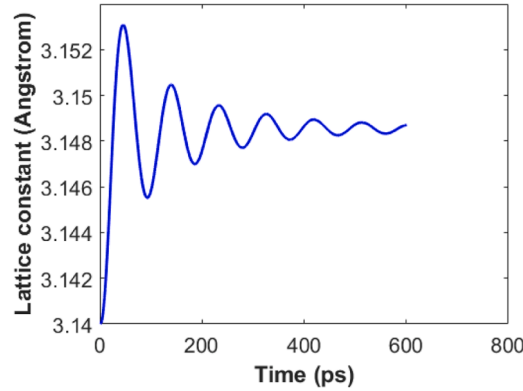


Fig. 6. Plot of change in lattice constant of perfect tungsten cell as it equilibrates at 300 K.

## Appendix B

The study predicting the He<sub>2</sub>V-SIA configuration does not clarify the position of the SIA relative to the He<sub>2</sub>V [5]. Thus, the BE for different positions of the SIA relative to the He<sub>2</sub>V is examined to identify a viable configuration. For example, for a vacancy created at co-ordinates [0,0,0], the SIA is positioned at [X,Y,Z], with X and Z ranging from 3.15 to 13.15 Å and -3.15 to -13.15 Å and Y ranging from 0.7 to 13.15 Å and from -0.7 to -13.15 Å (with incremental step-size of 0.2 Å). The lower limits for the ranges of X, Y and Z were chosen based on the minimum distance required to prevent the SIA from annihilating the vacancy upon relaxation.

For each considered position of the SIA relative to the He<sub>2</sub>V, the BE ( $E_{He_2V-SIA}^{BE}$ ) is calculated as per the following steps:

1. The formation energies of a He<sub>2</sub>V, a SIA and a He<sub>2</sub>V-SIA defect are calculated.
  - a. The following terms are considered for these calculations:
    - i.  $E_W$  is the energy of a single tungsten atom. Adding this component accounts for a SIA while subtraction of this component accounts for a removed tungsten atom i.e. a vacancy.
    - ii.  $E_{He}$  is the energy of an isolated helium ion.
    - iii.  $E_{pure}^{tot}$  is the total potential energy of a perfect tungsten cell.
    - iv.  $E_{He_2V}^{tot}$  is the potential energy of a tungsten cell with He<sub>2</sub>V defect.
    - v.  $E_{SIA}^{tot}$  is the potential energy of a tungsten cell with a SIA defect.
    - vi.  $E_{He_2V-SIA}^{tot}$  is the potential energy of a tungsten cell with a He<sub>2</sub>V-SIA defect.
  - b. The formation energy of a He<sub>2</sub>V defect ( $E_{He_2V}^{form}$ ), where a tungsten atom is removed (vacancy) and two helium ions are added.

$$E_{He_2V}^{form} = E_{He_2V}^{tot} - (E_{pure}^{tot} - E_W + 2E_{He})$$

- c. The formation energy of a SIA ( $E_{SIA}^{form}$ ), where a tungsten atom is added (a SIA).

$$E_{SIA}^{form} = E_{SIA}^{tot} - (E_{pure}^{tot} + E_W)$$

- d. The formation energy of a He<sub>2</sub>V-SIA ( $E_{He_2V-SIA}^{form}$ ), where a tungsten atom is removed (a vacancy), a tungsten atom is added (a SIA) and two helium ions are added).

$$E_{He_2V-SIA}^{form} = E_{He_2V-SIA}^{tot} - (E_{pure}^{tot} - E_W + E_W + 2E_{He})$$

2. The binding energy of the He<sub>2</sub>V-SIA is calculated using the above calculated formation energies as

$$E_{He_2V-SIA}^{BE} = E_{He_2V}^{form} + E_{SIA}^{form} - E_{He_2V-SIA}^{form}$$

3. Substituting the expressions for  $E_{He_2V}^{form}$ ,  $E_{SIA}^{form}$  and  $E_{He_2V-SIA}^{form}$  in this equation and simplifying gives

$$E_{He_2V-SIA}^{BE} = E_{He_2V}^{tot} + E_{SIA}^{tot} - E_{He_2V-SIA}^{tot} - E_{pure}^{tot}$$

For a cluster of He<sub>2</sub>V-SIA of size N, the BE was calculated as

$$E_{(\text{He}_2\text{V-SIA})_N}^{\text{BE}} = E_{(\text{He}_2\text{V})_N}^{\text{tot}} + E_{(\text{SIA})_N}^{\text{tot}} - E_{(\text{He}_2\text{V-SIA})_N}^{\text{tot}} - E_{\text{pure}}^{\text{tot}}$$

where,  $E_{\text{pure}}^{\text{tot}}$ ,  $E_{(\text{He}_2\text{V})_N}^{\text{tot}}$ ,  $E_{(\text{SIA})_N}^{\text{tot}}$  and  $E_{(\text{He}_2\text{V-SIA})_N}^{\text{tot}}$  are the total potential energy of a perfect tungsten cell, a tungsten cell with N He<sub>2</sub>V defects, a cell with N SIAs and a cell with N He<sub>2</sub>V-SIA defects respectively.

Fig. 1(j) shows the BE calculated for  $1 \leq N \leq 10$  cluster sizes. Small variations in the BE can be attributed to the variance of helium-vacancy complex across cluster sizes. For example, while both  $N = 3$  and  $N = 9$  clusters have 2 SIAs, the latter has slightly higher BE, owing to the larger strain field of its larger helium-vacancy complex (Fig. 1(d) and (h)).

### Appendix C

To create a simulation cell with an edge dislocation and periodic boundary conditions along the line direction (Y axis) and the Burgers' vector (X direction), the following steps were used:

1. A cell is created with double the intended height (Z-axis or the slip plane normal) i.e.  $X = 540 \text{ \AA}$  (with limits  $-270$  to  $270$ ),  $Y = 100 \text{ \AA}$  (with limits  $-50$  to  $50$ ) and  $Z = 540 \text{ \AA}$  (with limits  $-270$  to  $270$ ) is created.
2. Two edge dislocations, spanning across the Y-axis and located midway along the X-axis are introduced at  $Z = -135 \text{ \AA}$  and  $Z = 135 \text{ \AA}$ , respectively.
3. The cell is allowed to undergo potential energy minimisation with periodic boundary conditions applied along all directions.
4. The minimised cell is now cut into half along the Z direction i.e. only atoms in the region of  $Z > 0 \text{ \AA}$  are retained.
5. The cell with  $X = 540 \text{ \AA}$  (with limits  $-270$  to  $270$ ),  $Y = 100 \text{ \AA}$  (with limits  $-50$  to  $50$ ) and  $Z = 270 \text{ \AA}$  (with limits  $0$  to  $270$ ) is subject to potential energy minimisation again with periodic boundary conditions applied along the X and Y directions to obtain the simulation cell shown in Fig. 2(a).

### Appendix D

To determine the defect-dislocation interaction mechanism, a constant shear rate approach is used here where the block of immobile atoms at the top of cell are sheared at a constant rate while the block of the immobile atoms at the bottom of the cell are kept fixed (Fig. 2(a)). To examine the variation of pinning strength with applied shear rate, simulations with a range of shear rates were attempted for He<sub>2</sub>V-SIA defect cluster of size 3 placed in the path of the gliding edge dislocation (Fig. 2(a)).

For the highest shear rate attempted of  $0.003 \text{ ps}^{-1}$ , there was an unphysical rise in temperature within the cell, causing the atomic positions to become disorganised. Shear rate of  $0.0005 \text{ ps}^{-1}$  was also found to not show any distinguishable difference in the recorded shear stress, between the cases for with and without the defect in the dislocation path (with a peak stress of  $420 \text{ MPa}$  being reached in either case).

The pinning effect (i.e. a distinct difference in shear stress between the cases of with and without defect in the dislocation path) was first observed for a shear rate of  $0.0001 \text{ ps}^{-1}$ . Subsequently simulations at lower shear rates were attempted and the pinning strength was found to reduce with lowering shear rate before tending towards saturation for rates lower than  $10^{-6} \text{ ps}^{-1}$  (Fig. 7(a)). A polynomial fitting approach was used to fit the data points observed for the different shear rates (fitting line and corresponding equation in Fig. 7(a)). The equation determined from curve fitting was then used to estimate the pinning strength at a much lower shear rate of  $10^{-16} \text{ ps}^{-1}$  (i.e.  $10^{-4} \text{ s}^{-1}$  which corresponds to the strain rate used in the nano-indentation test in the prior study [14]). A small difference of  $\sim 2\%$  was noticed between the pinning strengths at rates  $10^{-6} \text{ ps}^{-1}$  and  $10^{-16} \text{ ps}^{-1}$ .

This indicates that values estimated from using a shear rate of  $10^{-6} \text{ ps}^{-1}$  have relatively little dependence on the shear rate. To further confirm this, simulations with He<sub>2</sub>V-SIA defect clusters of sizes 4 and 10, obstructing the gliding dislocation, were also attempted at rates  $10^{-4} \text{ ps}^{-1}$ ,  $10^{-5} \text{ ps}^{-1}$ ,  $10^{-6} \text{ ps}^{-1}$  and  $10^{-7} \text{ ps}^{-1}$  (Fig. 7 (c,d)). It is seen that, similar to the observation for cluster size 3, for cluster sizes 4 and 10 also, the pinning strength tends towards saturation below shear rate  $10^{-6} \text{ ps}^{-1}$ . Based on the polynomial curve fitting obtained for the cases of cluster size 4 and 10, the pinning strength at rate  $10^{-6} \text{ ps}^{-1}$ , was found to be within 2% of the interpolated value at rate  $10^{-16} \text{ ps}^{-1}$ . Based on these observations, all simulations in this study were performed at a constant shear rate of  $10^{-6} \text{ ps}^{-1}$ , to achieve an optimum balance between accuracy of results and computation time.

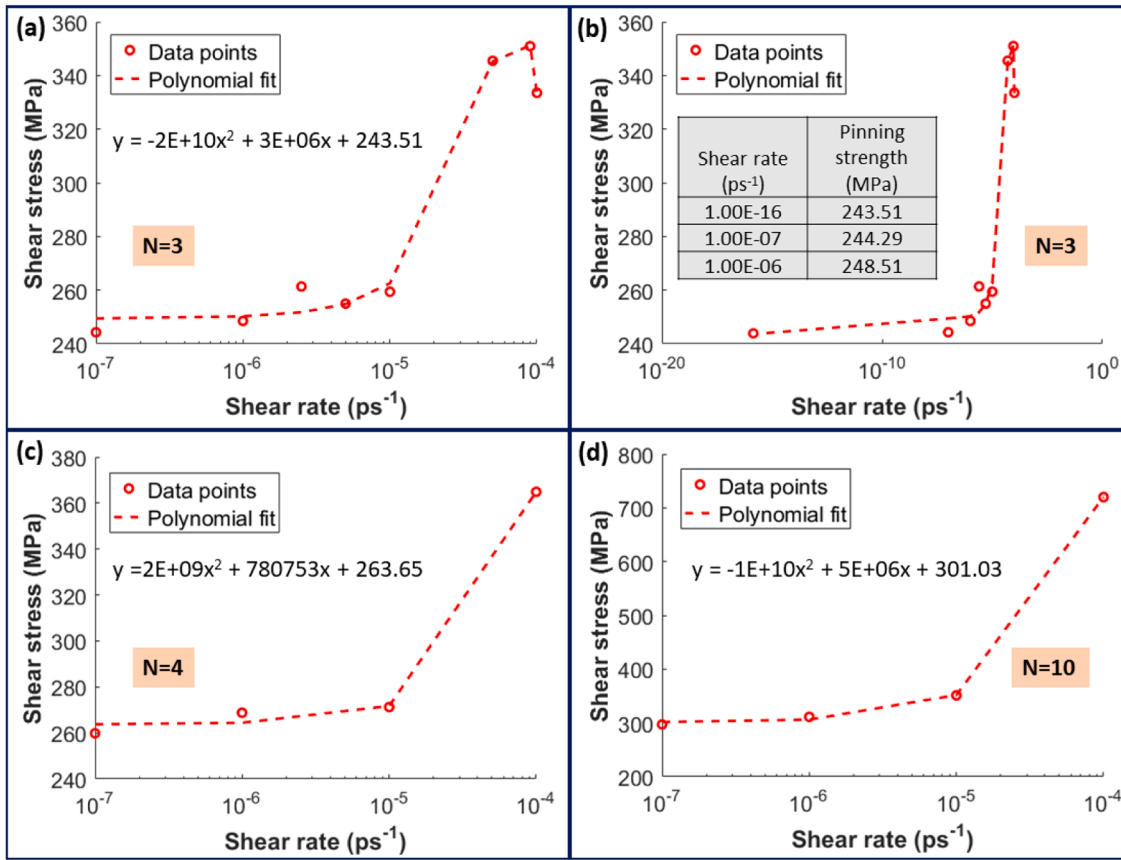


Fig. 7. Change of the pinning strength for He<sub>2</sub>V-SIA defect cluster of size 3, with the applied shear rate (a) data points observed at the examined shear rates superimposed by the polynomial fit with the equation stated in the inset and (b) subplot (a) shown with the polynomial fit interpolated to estimate the pinning strength for shear rate  $10^{-16} \text{ ps}^{-1}$ . Pinning strength observed at the examined shear rates superimposed by the polynomial fit with the equation stated in the inset for (c) He<sub>2</sub>V-SIA defect cluster of size 4 and (d) He<sub>2</sub>V-SIA defect cluster of size 10.

Appendix E

The pinning strength, i.e. the difference between the pinning force recorded for the defect-free case (averaged over the zone demarcated by the orange dotted line in Fig. 2(b)) and the maximum pinning force recorded with the defect present, varies as a function of the time over which the curves are averaged (Fig. 8). Fig. 8 shows that when the data is averaged over a period of 50 ps or more, the variation in the pinning strength diminishes and tends towards a saturated value of  $\sim 0.36 \mu\text{N}$ . Thus, an averaging time period of 100 ps is chosen and the uncertainty in the calculated pinning strength is measured as  $\pm 1$  standard deviation across the five values estimated by considering five different averaging time intervals, i.e. 20, 50, 100, 150 and 250 ps (Fig. 3(k) and Table 1).

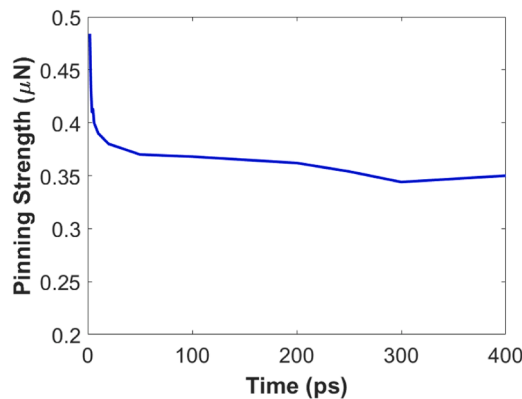


Fig. 8. Plot of pinning strength versus time over which curves are averaged.

Appendix F

The dimensions of the simulation cell are  $X = 540 \text{ \AA}$  (with limits  $-270$  to  $270$ ),  $Y = 100 \text{ \AA}$  (with limits  $-50$  to  $50$ ) and  $Z = 270 \text{ \AA}$  (with limits  $0$  to  $270$ ).

270). The cell contains 944,463 i.e. approximately a million atoms. Since the concentration of implanted helium is known to be 3000 appm, the simulation cell may be estimated to contain  $\sim 3000$  helium ions.

Considering uniform distribution of defects within the cell implies uniform spacing between defects. Let the spacing between defects be  $x$ .

Thus, number of defects along X, Y and Z directions is  $(540/x)$ ,  $(100/x)$  and  $(270/x)$  respectively.

For given cluster size  $N$ , the concentration of defect clusters will be  $B = 3000/A$  appm where  $A$  is the total number of helium ions in the cluster (Table 1).

Thus, total number of such clusters expected in the considered simulation cell is  $\sim B$ . Therefore,

$$(540/x) \times (100/x) \times (270/x) = B \quad (F1)$$

Eq. (F1) is used to compute the spacing between defects i.e.  $x$  for a given cluster concentration  $B$  as stated in the form of parameter  $C$  in Table 1.

The dislocation lies on the XY plane (Fig. 2(a)) and moves in the X direction. Thus, for a given cluster concentration  $B$ , at any point, the maximum number of defect clusters it may encounter will be  $(100/x)$  i.e. the ratio of the magnitude of the cell in the Y direction to the spacing between defects (stated as parameter  $D$  in Table 1).

## Appendix G

In Table 1 in the main text, the total solute hardening  $F_{tot}$  is computed for uniformly distributed defect clusters of varying size for 3000 appm of implanted helium. For each cluster size, the product of  $F_{tot}$  and the XY surface area of the simulation box gives the total solute strength ( $F_{sol}$  in  $\mu\text{N}$ ) for the given defect concentration. The simulation box will have moved by one Burgers' vector once the dislocation has traversed the full length of the box along the glide direction i.e. the X direction. Thus, the product of  $F_{sol}$  and the Burgers' vector gives the total energy required by the dislocation to cut through the defect concentration in its glide plane. This total energy divided by the total number of defect clusters encountered by the dislocation in the glide plane gives the average energy barrier of each defect  $E_{def}$ . The calculations for the same are shown in Table G.1 below. For the calculations in Table G.1, Burgers' vector value of  $2.7 \times 10^{-10}$  m is used [52].

**Table G.1**

Variation energy barrier of defect with cluster size of He<sub>2</sub>V-SIA defects.  $F_{tot}$  is as per calculations in Table 1 in the main text. The surface area of the XY face of the simulation box (Fig. 2(a)), used in the computation of  $F_{sol}$  is  $1.47 \times 10^{-15}$  m<sup>2</sup>. Details of calculation of parameters  $C$ ,  $D$  and  $E$  in Appendix F.

Cluster size (N)	Spacing between defects considering uniform distribution (C) in Å	Total solute hardening $F_{tot} = D \times F_1$ (MPa)	No. of defect clusters at any point along Y direction. $D = (100/C)$	No. of defect clusters at any point along X direction. $E = (540/C)$	Total number of defect clusters encountered in glide plane $Def_{tot} = D \times E$	Total solute strength ( $\mu\text{N}$ ) $F_{sol} = F_{tot} \times$ surface area of XY face of simulation box	Average energy barrier per defect (meV) $E_{def} = (F_{sol} \times b) / Def_{tot}$
3	30.87	750	3	17.4	52.48	1.102	0.035
4	33.98	810	3	15.89	47.68	1.19	0.04
5	36.61	900	3	14.75	44.25	1.32	0.05
6	38.9	810	3	13.88	41.64	1.19	0.048
7	40.95	600	2	13.18	26.37	8.82	0.056
8	42.82	580	2	12.61	25.22	8.526	0.057
9	44.53	540	2	12.12	24.25	7.938	0.055
10	46.12	620	2	11.71	23.42	9.114	0.066
							<b>Mean = 0.05</b>

## References

- [1] S. Das, Recent advances in characterising irradiation damage in tungsten for fusion power, SN. Appl. Sci. (2019), <https://doi.org/10.1007/s42452-019-1591-0>.
- [2] M. Rieth, et al., Recent progress in research on tungsten materials for nuclear fusion applications in Europe, J. Nucl. Mater. 432 (2013) 482–500.
- [3] R.G. Abernethy, Predicting the performance of tungsten in a fusion environment: a literature review, Mater. Sci. Technol. (United Kingdom) 33 (2017) 388–399.
- [4] I. De Broglie, C.E. Beck, W. Liu, F. Hofmann, Temperature dependence of helium-implantation-induced lattice swelling in polycrystalline tungsten: x-ray micro-diffraction and Eigenstrain modelling, Scr. Mater. 107 (2015) 96–99.
- [5] F. Hofmann, et al., Lattice swelling and modulus change in a helium-implanted tungsten alloy: x-ray micro-diffraction, surface acoustic wave measurements, and multiscale modelling, Acta Mater. 89 (2015) 352–363.
- [6] D.E.J. Armstrong, P.D. Edmondson, S.G. Roberts, Effects of sequential tungsten and helium ion implantation on nano-indentation hardness of tungsten, Appl. Phys. Lett. 251901 (2013) 1–5.
- [7] M.R. Gilbert, et al., An integrated model for materials in a fusion power plant: transmutation, gas production, and helium embrittlement under neutron irradiation, Nucl. Fusion 52 (2012) 083019.
- [8] K.D. Hammond, Helium, hydrogen, and fuzzi in plasma-facing materials, Mater. Res. Express. 4 (2017) 104002.
- [9] S. Das, et al., The effect of helium implantation on the deformation behaviour of tungsten: x-ray micro-diffraction and nanoindentation, Scr. Mater. 146 (2018) 335–339.
- [10] K.L. Murty, Chapter 3. Radiation damage, Fundam. Asp. Nucl. React. Elem. 59 (1975) 1–6.
- [11] B. Raj, M. Vijayalakshmi, P.R. Vasudeva Rao, K.B.S. Rao, Challenges in materials research for sustainable nuclear energy, MRS Bull. 33 (2008) 327–337.
- [12] C.E. Beck, S.G. Roberts, P.D. Edmondson, D.E.J. Armstrong, Effect of alloy composition & helium ion-irradiation on the mechanical properties of tungsten, tungsten-tantalum & tungsten-rhenium for fusion power applications, MRS Proc. 1514 (2013) 99–104.
- [13] J. Boisse, C. Domain, C.S. Becquart, Modelling self trapping and trap mutation in tungsten using DFT and molecular dynamics with an empirical potential based on DFT, J. Nucl. Mater. 455 (2014) 10–15.
- [14] S. Das, H. Yu, E. Tarleton, F. Hofmann, Hardening and strain localisation in helium-ion-implanted tungsten, Sci. Rep. 9 (2019) 1–14.
- [15] S. Sharafat, A. Takahashi, K. Nagasawa, N. Ghoniem, A description of stress driven bubble growth of helium implanted tungsten, J. Nucl. Mater. 389 (2009) 203–212.
- [16] A.M. Ito, Y. Yoshimoto, S. Saito, A. Takayama, H. Nakamura, Molecular dynamics simulation of a helium bubble bursting on tungsten surfaces, Phys. Scr. (T159) (2014) 014062.
- [17] K.D. Rasch, R.W. Siegel, H. Schultz, Quenching and recovery investigations of vacancies in tungsten, Philos. Mag. A 41 (1980) 91–117. *Physics of Condensed Matter, Structure, Defects and Mechanical Properties*.
- [18] H. Eleveld, A. van Veen, Deuterium interaction with impurities in tungsten studied with TDS, J. Nucl. Mater. 191–194 (1992) 433–438.
- [19] Kornelsen, E.V. Radiation effects the interaction of injected helium with lattice defects in a tungsten crystal the interaction of injected helium with lattice defects in a tungsten crystal. 13, 227–236 (1972).
- [20] P.E. Lhuillier, et al., Trapping and release of helium in tungsten, J. Nucl. Mater. 416 (2011) 13–17.
- [21] A. Debelle, M.F. Barthe, T. Sauvage, First temperature stage evolution of irradiation-induced defects in tungsten studied by positron annihilation spectroscopy, J. Nucl. Mater. 376 (2008) 216–221.
- [22] Z. Zhou, M.L. Jenkins, S.L. Dudarev, A.P. Sutton, M.A. Kirk, Simulations of weak-beam diffraction contrast images of dislocation loops by the many-beam Howie-Basinski equations, Philosophical Magazine 86 (2006) 4851–4881.

- [23] S.L. Dudarev, D.R. Mason, E. Tarleton, A.E. Sand, Multi-scale model for stresses, strains and swelling of reactor components under irradiation, *Nuclear Fusion* 58 (12) (2018) 126002.
- [24] L. Sandoval, D. Perez, B.P. Uberuaga, A.F. Voter, Competing kinetics and the bubble morphology in W, *Phys. Rev. Lett.* 114 (2015) 105502.
- [25] S. Das, W. Liu, R. Xu, F. Hofmann, Helium-implantation-induced lattice strains and defects in tungsten probed by X-ray micro-diffraction, *Mater. Des.* 160 (2018) 1226–1237.
- [26] F. Hofmann, et al., Non-contact measurement of thermal diffusivity in ion-implanted nuclear materials, *Sci. Rep.* 5 (2015) 16042.
- [27] N. Hashimoto, T.S. Byun, K. Farrell, S.J. Zinkle, Deformation microstructure of neutron-irradiated pure polycrystalline vanadium, *J. Nucl. Mater.* 336 (2005) 225–232.
- [28] T. Byun, N. Hashimoto, Strain localization in irradiated materials, *Nucl. Eng. Technol.* 38 (2006) 619–638.
- [29] S. Das, H. Yu, E. Tarleton, F. Hofmann, Orientation-dependent indentation response of helium-implanted tungsten, *Appl. Phys. Lett.* 114 (2019) 221905.
- [30] C.S. Becquart, M.F. Barthe, & De Backer, A. Modelling radiation damage and He production in tungsten, *Phys. Scr.* T145 (2011) 014048.
- [31] S. Das, H. Yu, K. Mizohata, E. Tarleton, F. Hofmann, Modified deformation behaviour of self-ion irradiated tungsten: a combined nano-indentation, HR-EBSD and crystal plasticity study, *Int. J. Plast.* 135 (2020) 102817.
- [32] D. Rodney, G. Martin, Dislocation pinning by small interstitial loops: a molecular dynamics study, *Phys. Rev. Lett.* 82 (1999) 3272–3275.
- [33] D. Rodney, G. Martin, Y. Bréchet, Irradiation hardening by interstitial loops: atomistic study and micromechanical model, *Mater. Sci. Eng. A* 309–310 (2001) 198–202.
- [34] D. Rodney, Molecular dynamics simulation of screw dislocations interacting with interstitial Frank loops in a model FCC crystal, *Acta Mater.* 52 (2004) 607–614.
- [35] H.L. Heinisch, F. Gao, R.J. Kurtz, Atomic-scale modeling of interactions of helium, vacancies and helium-vacancy clusters with screw dislocations in alpha-iron, *Philos. Mag.* 90 (2010) 885–895.
- [36] B.C. Masters, Dislocation Loops in Irradiated Iron, *Nature* 1963 200:4903 200 (1963), 254–254.
- [37] X. Yi, M.L. Jenkins, M.A. Kirk, Z. Zhou, S.G. Roberts, In-situ TEM studies of 150 keV W+ ion irradiated W and W-alloys: damage production and microstructural evolution, *Acta Mater.* 112 (2016) 105–120.
- [38] T.P. Remington, et al., Plastic deformation in nanoindentation of tantalum: a new mechanism for prismatic loop formation, *Acta Mater.* 78 (2014) 378–393.
- [39] A. Bakaev, D. Terentyev, P. Grigorev, M. Posselt, E.E. Zhurkin, Ab initio study of interaction of helium with edge and screw dislocations in tungsten, *Nucl. Instrum. Methods Phys. Res. B* 393 (2017) 150–154.
- [40] G. Bonny, P. Grigorev, D. Terentyev, On the binding of nanometric hydrogen-helium clusters in tungsten, *J. Phys. Condens. Matter* 26 (2014).
- [41] C.S. Becquart, C. Domain, An object kinetic Monte Carlo simulation of the dynamics of helium and point defects in tungsten, *J. Nucl. Mater.* 385 (2009) 223–227.
- [42] Y.N. Osetsky, D.J. Bacon, An atomic-level model for studying the dynamics of edge dislocations in metals, *Model. Simul. Mat. Sci. Eng.* 11 (2003) 427–440.
- [43] M. Ohring, *Mechanical behavior of solids*, *Eng. Mater. Sci.* 299–V (1995), <https://doi.org/10.1016/b978-012524995-9/50031-3>.
- [44] Anderson PM, Hirth JP, Lothe J. 2017 *Theory of Dislocations* - Peter M. Anderson, John P. Hirth, Jens Lothe - Google Books. 2024, 3rd edition. [https://books.google.co.uk/books?hl=en&lr=&id=LK7DDQAAQBAJ&oi=fnd&pg=PR19&dq=Anderson+PM,+Hirth+JP,+Lothe+J.+2017+Theory+of+dislocations.+Cambridge,+UK:+Cambridge+University+Press.&ots=OH4nrZkgWY&sig=v4\\_tJVgWuZdDS1gekGcU83UunN4&redir\\_esc=y#v=onepage&q=Anderson%20PM%2C%20Hirth%20JP%2C%20Lothe%20J.%202017%20Theory%20of%20dislocations.%20Cambridge%2C%20UK%3A%20Cambridge%20University%20Press.&f=false](https://books.google.co.uk/books?hl=en&lr=&id=LK7DDQAAQBAJ&oi=fnd&pg=PR19&dq=Anderson+PM,+Hirth+JP,+Lothe+J.+2017+Theory+of+dislocations.+Cambridge,+UK:+Cambridge+University+Press.&ots=OH4nrZkgWY&sig=v4_tJVgWuZdDS1gekGcU83UunN4&redir_esc=y#v=onepage&q=Anderson%20PM%2C%20Hirth%20JP%2C%20Lothe%20J.%202017%20Theory%20of%20dislocations.%20Cambridge%2C%20UK%3A%20Cambridge%20University%20Press.&f=false).
- [45] D.H. Thompson, E. Tarleton, S.G. Roberts, S.P. Fitzgerald, Interstitial-mediated dislocation climb and the weakening of particle-reinforced alloys under irradiation, *Phys. Rev. Mater.* 2 (2018) 080601.
- [46] J. Rösler, Particle strengthened alloys for high temperature applications: strengthening mechanisms and fundamentals of design, *Int. J. Mater. Product Technol.* 18 (2003) 70–90.
- [47] F.X. Liu, A.C.F. Cocks, E. Tarleton, Dislocation dynamics modelling of the creep behaviour of particle-strengthened materials, *Proc. R. Soc. A* 477 (2021), <https://doi.org/10.1098/rspa.2021.0083>.
- [48] K. Matsuura, The temperature dependence of work-hardening due to orowan loops in a dispersion-hardened alloy, *Trans. Jpn. Inst. Met.* 20 (1979) 395–403.
- [49] M. Huang, Z. Li, J. Tong, The influence of dislocation climb on the mechanical behavior of polycrystals and grain size effect at elevated temperature, *Int. J. Plast.* 61 (2014) 112–127.
- [50] K. Danas, V.S. Deshpande, Plane-strain discrete dislocation plasticity with climb-assisted glide motion of dislocations, *Model. Simul. Mat. Sci. Eng.* 21 (2013) 045008.
- [51] C. Ayas, J.A.W. Van Dommelen, V.S. Deshpande, Climb-enabled discrete dislocation plasticity, *J. Mech. Phys. Solids.* 62 (2014) 113–136.
- [52] B.N. Dutta, B. Dayal, Lattice constants and thermal expansion of palladium and tungsten up to 878 C by X-ray method, *Physica Status Solidi* 3 (1963) 2253–2259 (b).